PCCP

Femtosecond Intersystem Crossing to the Reactive Triplet State of the 2,6-Dithiopurine Skin Cancer Photosensitizer

Journal:	*Physical Chemistry Chemical Physics*
Manuscript ID	CP-ART-09-2021-004415
Article Type:	Paper
Date Submitted by the Author:	26-Sep-2021
Complete List of Authors:	Ortiz-Rodríguez, Luis; Case Western Reserve University College of Arts and Sciences, Chemistry Hoehn, Sean; Case Western Reserve University College of Arts and Sciences, Chemistry Acquah, Chris; Case Western Reserve University College of Arts and Sciences, Chemistry Abbass, Nadia; Case Western Reserve University College of Arts and Sciences, Chemistry Waidmann, Lidia; Case Western Reserve University College of Arts and Sciences, Chemistry Crespo-Hernández, Carlos; Case Western Reserve University College of Arts and Sciences, Chemistry

ARTICLE

Femtosecond Intersystem Crossing to the Reactive Triplet State of the 2,6-Dithiopurine Skin Cancer Photosensitizer

Received 00th January 20xx,
Accepted 00th January 20xx

DOI: 10.1039/x0xx00000x

Luis A. Ortiz-Rodríguez,[a] Sean J. Hoehn,[a] Chris Acquah,[a] Nadia Abbass,[a] Lidia Waidmann,[a] and Carlos E. Crespo-Hernández*[,a]

Site-selected sulfur-substituted nucleobases are a class of all organic, heavy-atom-free photosensitizers for photodynamic therapy applications that exhibit excellent photophysical properties such as strong absorption in the ultraviolet-A region of the electromagnetic spectrum, near-unity triplet yields, and high yield of singlet oxygen generation. Recent investigations on doubly thionated nucleobases, 2,4-dithiothymine, 2,4-dithiouracil, and 2,6-dithiopurine, demonstrated that these set of dithionated nucleobases outperform the photodynamic efficacy exhibit by 4-thiothymidine–the most widely studied singly substituted thiobase to date. Out of the three dithionated nucleobases, 2,6-dithiopurine was shown to be the most effective, exhibiting inhibition of cell proliferation of up to 63% when combined with a low UVA dose of 5 J cm^{-2}. In this study, we elucidated the electronic relaxation pathways leading to the population of the reactive triplet state of 2,6-dithiopurine. 2,6-Dithiopurine populates the triplet manifold in less than 150 fs, reaching the nπ* triplet state minimum within a lifetime of 280 ± 50 fs. Subsequently, the population in the nπ* triplet state minimum, internally converts to the long-lived ππ* triplet state within a lifetime of 3 ± 1 ps. The relatively slow internal conversion lifetime is associated to major conformational relaxation in going from the nπ* to ππ* triplet state minimum. A unity triplet yield of 1.0 ± 0.1 is measured.

Introduction

Skin cancers (i.e., basal, squamous, and melanoma) are ubiquitous around the world.[1–3] About 65,000 people worldwide die of nonmelanoma skin cancer every year.[4] Standard treatments against skin cancers include surgery, radiotherapy, and chemotherapy. In recent years, photodynamic therapy (PDT) has grown in popularity,[5,6] due to its excellent spatiotemporal selectivity and diminished side effects[7,8] compared to the aforementioned standard treatments. PDT relies on the administration of a photosensitizer (PS) that generates singlet oxygen (i.e., Type II photosensitization reaction)[9] and other reactive oxygen species (i.e., Type I)[9] upon photoactivation, which are toxic to the targeted malignancies.[10] However, PDT still lacks optimal PSs that are applicable in a broad spectrum of malignancies. Some of the challenges encountered in the development of optimal PSs are: (1) understanding of the deactivation mechanisms, (2) need for high triplet and singlet oxygen generation yields, (3) and the important consideration that the efficacy of a PS is dictated not only by the type of targeted cell and their oxygenation status, but its ability to penetrate the malignant tissue and the wavelength required for photoactivation of the PS.[11]

Site-selected sulfur-substituted nucleobases (a.k.a., thiobases) are a class of heavy-atom-free PSs for PDT applications.[10,12] In the thiobases, a sulfur atom replaces the oxygen atom of an exocyclic carbonyl group. Thionation of the nucleobases has a significant impact on their photophysical and photochemical properties.[10,12–16] For example, the single-atom substitution converts most of the nucleobases into effective ultraviolet-A (UVA: 320-400 nm, $\varepsilon \geq 10^4$ $M^{-1}cm^{-1}$) absorbers. 4-thiothymidine (4tThd) is the thiobase that has been studied the most for prospective PDT applications.[17–20] The photodynamic efficacy of 4tThd with non-toxic UVA radiation doses has been demonstrated against a variety of cancer cell lines such as human fibroblasts, keratinocytes, squamous carcinoma cells, and bladder cancer cells.[17–20] Even though 4tThd is a promising PS, ideally the PS should absorb at longer wavelengths because longer wavelengths penetrate deeper into tissues, allowing PDT treatment at much greater depths.

Recent fundamental investigations by our research group have provided valuable insight into the enhancement of the photodynamic potential of the thiobases.[21,22] Specifically, the effect of site and degree of thionation was investigated in 2,4-dithiothymine (dtThy) and 2,4-dithiouracil (dtUra).[21,22] In these investigations, it was found that by doubling the thionation of the thiobases, the absorption spectrum can be redshifted to even longer UVA wavelengths, while preserving their large absorption coefficients. This allows for deeper tissue penetration. It was also demonstrated that the rate of triplet state population can be increased relative to their singly

[a] Department of Chemistry, Case Western Reserve University, Cleveland, OH 44106.
* Corresponding author; E-mail: carlos.crespo@case.edu; ORCID: 0000-0002-3594-0890

† Electronic Supplementary Information (ESI) available: Steady-state emission data; optimized geometries of deprotonated of deprotonated tautomers of 2,6-Dithiopurine and femtosecond transient absorption data upon excitation with 342 nm.
See DOI: 10.1039/x0xx00000x

thionated counterparts.[21,22] Following these investigations, the photosensitizing activities of dtThy, dtUra, and 2,6-dithiopurine (dtPur) were also studied and it was demonstrated that these compounds can effectively decrease the proliferation of epidermoid carcinoma cells *in vitro* upon activation with a low UVA dose (5 J cm^{-2}).[23] It was shown that the most effective PSs is dtPur, exhibiting inhibition of cell proliferation of up to 63% when dtPur (300 μM) was combined with a UVA dose of 5 J cm^{-2}. Interestingly, the increased efficacy of dtPur against epidermoid carcinoma cells did not correlate with the generation of reactive oxygen species (ROS) but correlated with the magnitude of the decay lifetime of their excited triplet state. While dtThy and dtUra have similar triplet decay lifetime, dtPur exhibits a two-fold longer lifetime. Hence, it was proposed that ROS generation are important but do not play a key role in the observed efficacy of dtPur against skin cancer cell proliferation. It was proposed that direct reactions of the triplet state of dtPur with biomolecules in the cell could be playing an important role. Therefore, it was shown that dtPur can photosensitized damage to cells in both oxygenated and O_2-deficient tissues. Importantly, however, the electronic relaxation pathways leading to the population of the reactive triple state of dtPur have not been studied.

In this study, steady-state absorption and emission spectroscopy and broadband transient absorption spectroscopy are complemented with density functional theory (DFT) and time dependent density functional theory (TD-DFT) to characterize the photophysical, photochemical, and electronic structure properties of dtPur, with a focused attention on the pathways leading to the population of the long-lived reactive triplet state.

Experimental and Theoretical Methods

Chemicals and steady-state measurements

2,6-dimercaptopurine (>98% purity), also known as 2,6-dithiopurine, was obtained from Tokyo Chemical Industry America (TCI America) and used as received. Phosphate buffer with total phosphate concentration of 16 mM was freshly prepared using monobasic sodium phosphate and dibasic sodium phosphate dissolved in 250 mL of ultrapure water and adjusted to pH 7.4 using a 0.1 M NaOH solution. Steady-state absorption and emission spectroscopy were performed using a Cary 300 Bio and Cary Eclipse spectrometers, respectively. Fluorescence spectra were taken at PMT voltage of 800 V with slit widths of 5 nm.

Broadband transient absorption spectroscopy

The transient absorption setup used in this work is described in detail elsewhere.[24] Briefly, a Ti:Spapphire oscillator (Vitesse, Coherent, Santa Clara, CA, USA) seed a regenerative amplifier (Coherent Libra-HE) that generates pulses of a 100 fs (1 kHz and 800 nm). A fraction of the beam is used to pump a Traveling Optical Parametric Amplifier of Superfluorescence (TOPAS, Quantronix/Light Conversion, Vilnius, Lithuania), while the other portion is focused on a translating 2 mm CaF_2 crystal to generate the white light continuum for probing (ca. 320 to 700 nm). In this work, the TOPAS was tuned to 325 and 342 nm. The femtosecond to nanosecond measurements were done employing a mechanical delay stage with a temporal limit of 3 ns and the nanosecond to microseconds measurements were done employing an electronically triggered white light source (Eos, Ultrafast Systems, LLC, Sarasota, FL, USA). The excitation pulses were set to a power of 1.75 mW (measured at the optical cell position) using a neutral density filter. A 2 mm quartz optical cell was used for all measurements. To ensure irradiation of fresh volume, the solution was continuously stirred with a Teflon-coated magnetic bar. All solutions were kept below 3 % degradation, as judged from the absorption maximum of the lowest-energy absorption band of 2,6-dithiopurine at 348 nm.

Global and target analyses of the femtosecond transient data were performed using the Glotaran software package, where the transient data was fit with a three-component sequential kinetic model.[25]The nanosecond data was fit using a global analysis subroutine in Igor Pro 6.37 (Wavemetrics, Inc). The decay traces obtained from nanosecond transient absorption spectroscopy (ns-TAS) data were fit with a single exponential function convoluted with a Gaussian instrument response function of 400 ps (FWHM). The extinction coefficient for triplet-triplet absorption band and the triplet yield of dtPur were obtained by using the singlet depletion method[26] and the relative actinometry method,[26] respectively. 6-thioguanosine (6tGuo) was used as the triplet yield (80%) standard. [27]

The data collected exciting at 342 nm is reported in the ESI because the stimulated Raman signal of the solvent appears on top of relevant transient species, making difficult their analysis. However, the data collected exciting at 342 nm was used for the triplet yield calculations because it exhibits a clean bleaching signal, which is necessary for the singlet-depletion method to be applicable.

Electronic structure calculations

All the optimizations and vertical excitation energies were performed using Gaussian 16 suite of programs.[28] Spin-orbit coupling constants and excited state absorption spectra were obtained in ORCA 4.2.1.[29] Solvation effects were modelled implicitly in Gaussian 16 or in ORCA 4.2.1 by means of the integral equation formalism of the polarizable continuum model (IEFPCM)[30] or the conductor-like polarizable continuum model (CPCM),[31] respectively. To model solvation effects explicitly, water molecules were added strategically to form hydrogen bonds with the nitrogen atoms of the purine chromophore. The ground-state geometries were optimized with density functional theory (DFT) using the B3LYP functional[32,33] and the 6-311+G(d,p) standard basis set. The relative energies among tautomers were calculated at the MP2 level of theory using the DFT-optimized structures. The optimized ground state geometries were then used to obtain the vertical excitation energies (VEEs) using time-dependent density functional theory (TD-DFT) with the PBE0[34] functional and the 6-311+G(d,p) standard basis set. Characters of the excited states were assigned by considering the magnitude of

the oscillator strengths and by visual inspection of the Kohn-Sham orbitals. The excited states were optimized in water with TD-DFT using the PBE0 functional and the 6-311+G(d,p) basis set. All geometries were optimized without constraints. Spin-orbit coupling were obtained at the TD-PBE0/CPCM/6-311+G(d,p) using the optimized geometry of the lowest-energy singlet state. In order to construct the potential energy profiles, all the energies were obtained using the PBE0 and the 6-311+G(d,p) basis set.

Results

Steady state photophysics

dtPur consists of a purine core chromophore thionated at the C2 and C6 positions (inset, Figure 1). dtPur has two pK_a values: a pK_1 of 5.08 and a pK_2 of 10.06.[35] The Henderson-Hasselbalch relationship was used to determine the ratio of neutral and the conjugated base (deprotonated) of dtPur at physiological pH. Based on this calculation, dtPur exists (>99%) as the deprotonated species at physiological pH and thus, from this point forward we focus our investigations on its deprotonated form.

Figure 1 shows the molar absorption spectrum of dtPur in phosphate buffer pH 7.4. The two lowest energy absorption bands have maxima at 348 (16.5 ± 0.5 mM^{-1} cm^{-1}) and 287 nm (26.6 ± 0.5 mM^{-1} cm^{-1}). Figure S1a show that two low-intensity emission bands, one centered at 425 nm and the other one centered at 518 nm, are observed at pH 7.4. The intensity of the emission band centered at 535 nm increases under N_2-saturated condition, while the band centered at 425 nm is independent of the molecular oxygen concentration. Therefore, the band centered at 535 nm is assigned to phosphorescence, while the band centered at 425 nm is assigned to fluorescence. The excitation spectrum taken at an emission wavelength of 535 nm (Figure S1b) is in good agreement with the absorption spectrum of dtPur, evidencing that the detected emission is from dtPur and not from an impurity. Collection of the excitation

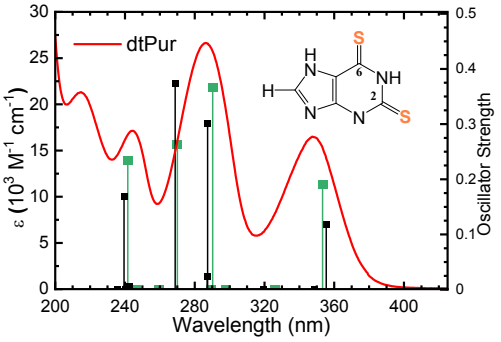

Figure 1. Molar absorption spectrum of dtPur in phosphate buffer pH 7.4. Black and green vertical lines correspond to the calculated electronic transitions and corresponding oscillator strengths at the TD-PBE0/IEFPCM/6-31+G(d,p)//B3LYP/IEFPCM/6-31+G(d,p) in water for microsolvated and non-microsolvated geometries, respectively. Inset: molecular structure of the most stable tautomer of dtPur according to the electronic-structure calculations reported in this study in water.

spectrum at an emission wavelength of 425 nm was attempted without success due to the extremely low signal. Fluorescence and phosphorescence quantum yields cannot not determined with accuracy because the emission signals are within the detection limit of the spectrofluorometer. However, we can estimate emission quantum yields in the order of 10^{-4}, as observed for the other thiobases.[12]

Prototropic tautomerization of deprotonated dtPur

As mentioned above, dtPur exists in its deprotonated form (>99%) at physiological pH. Considering that purine derivatives often exhibit prototropic tautomerization,[36–38] 21 different tautomers were considered and optimized at the B3LYP/IEFPCM/6-311+G(d,p) level of theory in water (Figure S2). According to these calculations, the only two tautomers that are predicted to be available at room-temperature are the N7(H)-N1(H) and N9(H)-N1(H) tautomers. Further optimizations of these tautomers with two explicit water molecules forming hydrogen bonds with the nitrogen atoms of the purine core, and subsequent single-point calculations at the MP2 level of theory, predict that the relative energy among these tautomers is 1.25 kcal/mol, where the N7(H)-N1(H) tautomer is the most stable (Figure S3). Because the relative energy between the most stable tautomer and the second most stable tautomer is well-above *kT*, only the N7(H)-N1(H) tautomer is expected to be available in solution. Therefore, all calculation presented hereafter were performed exclusively for the N7(H)-N1(H) tautomer.

Vertical excitation energies

Vertical excitation energies (VEE) were calculated at the TD-PBE0/IEFPCM/6-311+G(d,p) in water both in the non-microsolvated and microsolvated geometries of the N7(H)-N1(H) tautomer of the deprotonated dtPur (Table 1) to characterize the electronic states available upon UVA excitation. The first excited singlet state is predicted to be directly populated upon UVA excitation at 325 nm. This state has ππ* character with significant oscillator strength (>0.1). Below the ^{1}ππ* state, there are three triplet excited states available for deactivation in the Franck-Condon region. The highest energy triplet state has nπ* character, while the two-lowest energy triplet states have ππ* character. We remark that microsolvation of deprotonated dtPur does not significantly impact the VEE at this level of theory, as shown in Table 1.

Excited states optimizations, spin-orbit coupling constants, potential energy profiles and excited states absorption spectra

According to the VEE reported in the previous section, four excited electronic states may participate in the electronic relaxation mechanism of deprotonated dtPur upon UVA excitation. Hence, the nuclear coordinates of all four excited states were optimized at the TD-PBE0/IEFPCM/6-311+G(d,p) level of theory. The optimized geometries are presented in Figure 2. Both the ^{1}ππ* and lowest energy ^{3}ππ* states minima

Table 1. Vertical excitation energies (in eV) of non-microsolvated and microsolvated dtPur calculated at the TD-PBE0/IEFPCM/6-311+G(d,p) level of theory in water.

State	IEFPCM	IEFPCM+ $2H_2O$
($^1\pi\pi^*$)	3.41 (0.191)	3.39 (0.120)
($^3\pi\pi^*$)	2.47	2.56
($^3\pi\pi^*$)	3.00	3.27
($^3n\pi^*$)	3.40	3.36

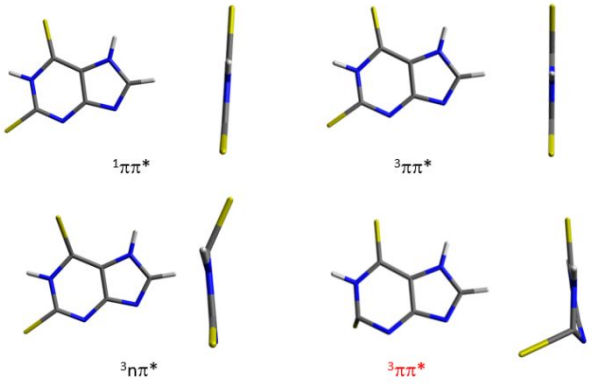

Figure 2. Optimized excited state geometries of relevant excited states of deprotonated dtPur at the TD-PBE0/IEFPCM/6-311+G(d,p) level of theory in water. Note: the second lowest-energy $^3\pi\pi^*$ was labelled in red to differentiate it from the lowest-energy $^3\pi\pi^*$.

consist of planar geometries, while the second lowest-energy $^3\pi\pi^*$ and the $^3n\pi^*$ minima consist of significantly distorted geometries. Following optimization of the excited states, we noted that the $^3n\pi^*$ state becomes lower in energy than the second lowest energy $^3\pi\pi^*$ state. The optimized Franck-Condon and $^1\pi\pi^*$ state geometries were used to calculated the spin-orbit coupling constants (SOCs) between the $^1\pi\pi^*$ state and the triplet states in water at the TD-PBE0/CPCM/6-311+G(d,p) level of theory. The SOC between the $^1\pi\pi^*$ and $^3n\pi^*$ are 88 and 116 cm^{-1} at the Franck-Condon region and $^1\pi\pi^*$ minimum, respectively. The SOCs between the $^1\pi\pi^*$ and the lowest- and second lowest-energy $^3\pi\pi^*$ state at the Franck-Condon region are 4 and 8 cm^{-1}, respectively, while at the $^1\pi\pi^*$ minimum geometry they are 0.02 and 0.01 cm^{-1}, respectively. The magnitude of the SOC between the $^1\pi\pi^*$ and $^3n\pi^*$ is in good agreement with El-Sayed's propensity rules,[39] given the fact that this transition involves a change of orbital type. Considering the SOCs and the fact that following optimization the $^3n\pi^*$ becomes lower in energy than the second lowest-energy $^3\pi\pi^*$ state, it is proposed that the second lowest-energy $^3\pi\pi^*$ state does not play a primary role in the relaxation mechanism of deprotonated dtPur in solution. Therefore, this state is not included in the potential energy profiles presented

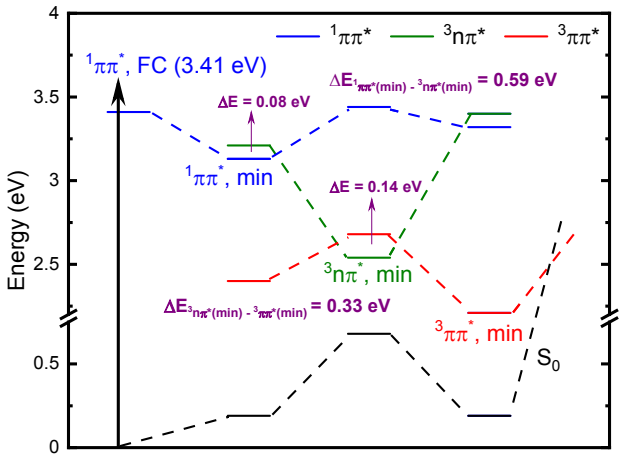

Figure 3. Potential energy profiles of relevant excited states of deprotonated dtPur available upon UVA excitation obtained at the TD-PBE0/IEFPCM/6-311+G(d,p) level of theory in water. $\Delta E^1_{\pi\pi^*(min) - {}^3n\pi^*(min)}$ and $\Delta E^3_{n\pi^*(min) - {}^3\pi\pi^*(min)}$ represent the energy gaps between the optimized minima of the $^1\pi\pi^*$ and $^3n\pi^*$ states and $^3n\pi^*$ state and $^3\pi\pi^*$, respectively.

in Figure 3. In a nutshell, based on the electronic structure calculations reported in this section, it can be proposed that UVA excitation of dtPur leads to population of the $^1\pi\pi^*$ state in aqueous solution, which can rapidly intersystem cross to the triplet manifold from the $^1\pi\pi^*$ state to the $^3n\pi^*$ state and subsequently, internally convert to the lowest-energy $^3\pi\pi^*$ state. Taking into account the magnitude of the SOCs and the small energy gap (ΔE=0.08 eV, Figure 3) between the $^1\pi\pi^*$ and the $^3n\pi^*$ states at the $^1\pi\pi^*$-minimum geometry, the intersystem crossing event is expected to occur on an ultrafast timescale, as observed for the other thionated nucleobases.[12,21,22,40,41] The excited state absorption spectra of the relevant $^1\pi\pi^*$, $^3n\pi^*$ and $^3\pi\pi^*$ states were also calculated at the TD-PBE0/CPCM/6-311+G(d,p) level of theory in water and are reported in Figure 4.

Transient absorption spectroscopy

Femtosecond transient absorption experiments were performed to investigate the electronic relaxation channels of deprotonated dtPur and to quantify their rates. Figure 5 presents the transient absorption spectra upon excitation with 325 nm. As can be seen in Figure 5a, two transient bands are observed within the cross-correlation of the pump and probe beams. One has a maximum at 393 nm and blueshifts to 386 nm during the initial 0.17 ps, while the other has a maximum at 575 nm and blueshifts to 480 nm during the initial 0.17 ps. From 0.17 to 0.64 ps, the amplitude of the band with maximum at 386 nm increases, while the band with maximum at 480 nm blueshifts to ca. 460 nm with simultaneous increase in intensity (Figure 5b). From 0.64 ps to 128 ps, the amplitude of the higher-energy band with maximum at 386 nm decreases, while the band at ca. 460 nm continues to grow, forming an apparent isosbestic point around 420 nm (Figure 5c). In Figure 5d, it can be observed that the dynamics after a time delay of 128 ps stay practically

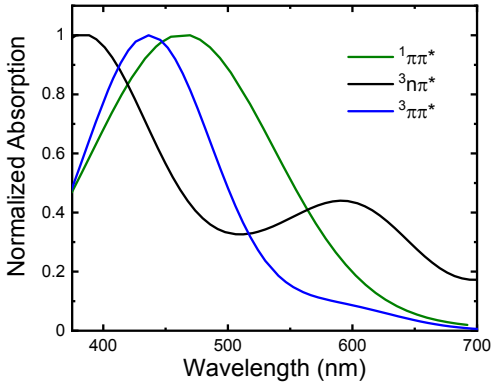

Figure 4. Calculated excited state absorption spectra of the relevant $^1\pi\pi^*$, $^3n\pi^*$ and $^3\pi\pi^*$ states at the TD-PBE0/CPCM/6-311+G(d,p) level of theory in water. The transitions were convoluted with a Gaussian function with FWHM= 60 nm.

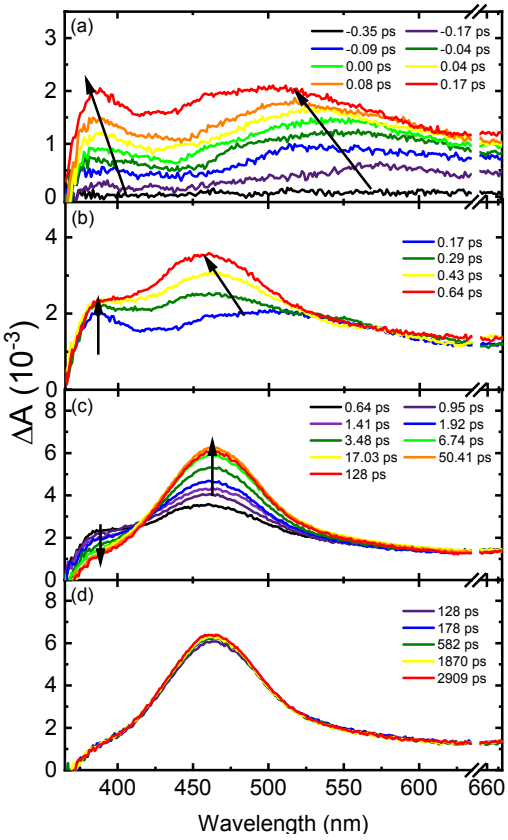

Figure 5. Transient absorption spectra of dtPur in phosphate buffer pH 7.4 upon excitation with 325 nm. Breaks cover the scattering of the pump beam reaching the detectors. Black arrows are used to guide the eye. Time zero was defined as the point where the decay trace at 550 nm reaches half of its maximum amplitude.

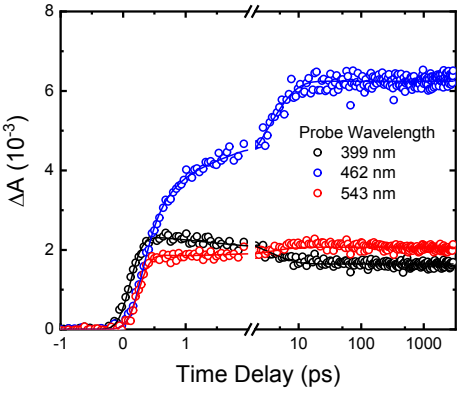

Figure 6. Representative decay traces at key probe wavelengths of dtPur in phosphate buffer pH 7.4.

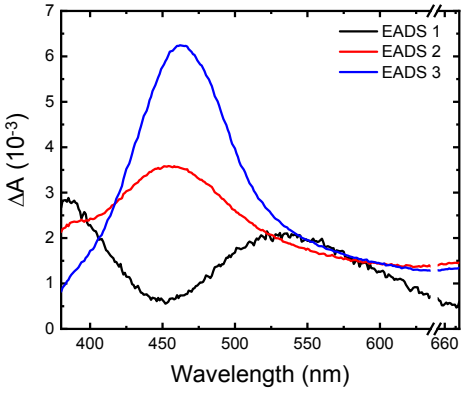

Figure 7. Evolution-associated difference spectra extracted from the global and target analyses of the transient data with a 3-component sequential kinetic model. Breaks cover the scattering of the pump beam reaching the detectors.

Table 2. Photophysical properties of dtPur in phosphate buffer pH 7.4.

$\lambda_{exc.}$	τ_1 (fs)	τ_2 (ps)	τ_3 (ns)	ε_T ($mM^{-1}cm^{-1}$)	ϕ_T	τ_T (μs)
325 nm	280 ± 50	3 ± 1	>> 3 ns	14.0 @ 462 nm	1.0 ± 0.1	0.56 ± 0.02[a]
342 nm	280 ± 45	3 ± 1				4.0 ± 0.1[b]

[a] measured in air-saturated conditions; [b] measured in nitrogen-saturated conditions [e]

constant, confirming a population that last longer than 3 ns. Lifetimes, representative decay traces, and evolution-associated difference spectra (EADS) extracted from the global and target analyses are reported in Table 2, Figure 6, and Figure 7, respectively.

Nanosecond transient absorption experiments were performed under air- and N_2-saturated conditions to measure the dynamics at longer than 3 ns. The decay traces were fit adequately to a single exponential convoluted with a Gaussian instrument response function with FWHM = 400 ps (Figure 8). The lifetimes obtained under air- and N_2-saturated conditions are listed in Table 2. The

lifetimes were obtained by averaging 35 traces in the probe spectral range from 440 to 480 nm to increase the signal to noise ratio.

Discussion

The EADS (Figure 7) extracted from the global and target analysis satisfactorily captures all the key features observed in the spectral evolution of the transient data reported in Figure 5. Therefore, is expected that a comparison of the EADS with the calculated absorption spectra of the $^1\pi\pi^*$, $^3n\pi^*$ and $^3\pi\pi^*$ states should provide crucial information about the states involved in the deactivation mechanism of deprotonated dtPur. Figure 9 compares the normalized EADS extracted from the global and target analyses of the transient data with the calculated excited state absorption spectra of the $^1\pi\pi^*$, $^3n\pi^*$, $^3\pi\pi^*$ and a linear combination of the $^3n\pi^*$and $^3\pi\pi^*$ states. Considering this comparison, we assigned the transient species that appears within the cross-correlation of the pump and probe beams to the absorption spectrum of the $^3n\pi^*$ state, the dynamics observed in EADS2 to the linear combination of the $^3n\pi^*$and $^3\pi\pi^*$ states absorption spectra and the long-lived transient species (EADS 3) to the absorption spectrum of the $^3\pi\pi^*$ state.

No clear evidence of the excited state absorption spectrum of $^1\pi\pi^*$ state is observed in our transient data, which suggests that intersystem crossing to the $^3n\pi^*$ state occur in a faster timescale than the IRF of the spectrometer used in this work (i.e., 150 fs). These results confirm that the intersystem crossing event between the $^1\pi\pi^*$ and $^3n\pi^*$ states occur in an ultrafast fashion as predicted by the SOCs and the small energy gap (ΔE = 0.08 eV, Figure 3) between the states at the $^1\pi\pi^*$-minimum geometry obtained with the electronic-structure calculations. It is expected that the intersystem event to occur in < 150 fs, considering that an intersystem crossing lifetime of ca. 150 fs has been reported for other thiobases, such as 2-thiouracil, 2-4-dithiouracil and 4-thiouracil.[41] Furthermore, the triplet yield measured in this study for the the deprotonated dtPur (1.0 ± 0.1) is higher than for any of those thiobases.[21,22] The unity triplet yield is also consistent with the observation of room-temperature phosphorescence and a 19% singlet oxygen quantum yield.[23] The blueshift observed in Figure 5a is assigned to conformational relaxation of the $^3n\pi^*$ state from a nearly-planar conformation to a out-of-plane geometry that characterizes its minimum (Figure 2). Hence, τ_1 is assigned to conformational relaxation in the $^3n\pi^*$ state. Note that the apparent isosbestic point observed in Figure 5c is assigned to internal conversion from the $^3n\pi^*$ state to the $^3\pi\pi^*$ state and thus, τ_2 (3 ± 1 ps) corresponds to this process with the possibility of simultaneous vibrational cooling in the $^3\pi\pi^*$ state. We propose that the internal conversion from the $^3n\pi^*$ state to the $^3\pi\pi^*$ state occurs with a lifetime of 3 ps due to a major conformational change (i.e., going from severely distorted ring geometry in the $^3n\pi^*$ state to a planar $^3\pi\pi^*$ state, Figure 2). After its population, the $^3\pi\pi^*$ state decays with a lifetime of 0.56 and 4.0 μs in air- and N_2-saturated conditions, respectively, suggesting small SOCs for

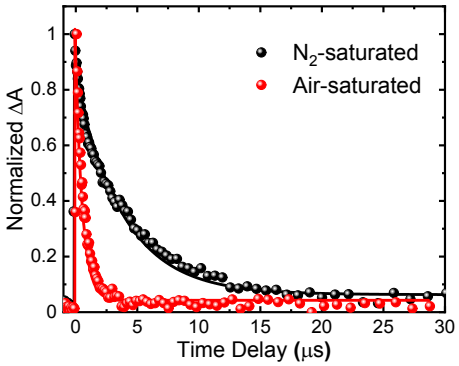

Figure 8. Representative triplet-decay traces measured for dtPur in phosphate buffer pH 7.4 under air- and N_2-saturated conditions following excitation at 325 nm. The fit obtained from a global analysis of the broadband transient data are also presented as solid lines. The decay traces shown are the results of the average of 35 traces in the probe spectral range from 440 to 480 nm.

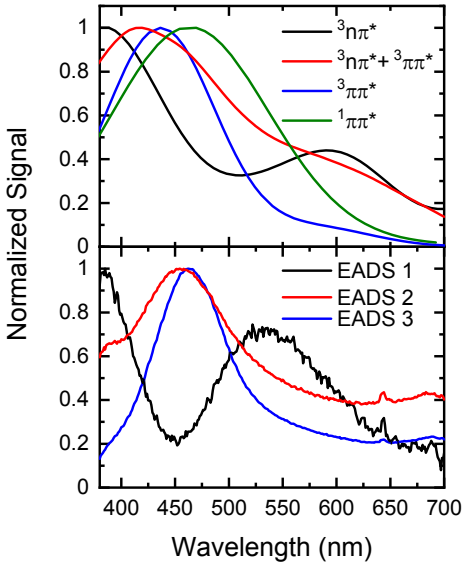

Figure 9. Normalized evolution-associated difference spectra extracted from the global and target analyses of the transient data of dtPur and normalized calculated excited state absorption spectra of the $^1\pi\pi^*$, $^3n\pi^*$, $^3\pi\pi^*$ and a linear combination of the $^3n\pi^*$and $^3\pi\pi^*$ states.

intersystem crossing to the ground state and/or a relatively high energy barrier to access the $^3\pi\pi^*/S_0$ crossing region. The $^3\pi\pi^*$state can also sensitized the generation of singlet oxygen with a quantum yield of 19%.[23] The proposed deactivation mechanism for deprotonated dtPur is summarized in Scheme 1. The $^3\pi\pi^*$ state can also sensitized the generation of singlet oxygen with a quantum yield of 19%.[23] The proposed deactivation mechanism for deprotonated dtPur is summarized in Scheme 1.

Conclusions

In this contribution, steady-state and time-resolved spectroscopies were complemented with electronic-structure calculations to provide a detailed electronic relaxation mechanism for the skin cancer photosensitizer dtPur in phosphate buffer at pH 7.4. The deprotonated dtPur is the thiobase with the highest photodynamic efficacy[23] and triplet yield reported thus far. Scheme 1 summarizes the deactivation mechanism. It is proposed that UVA excitation to the $^1\pi\pi^*$ state leads to ultrafast intersystem crossing to the triplet manifold through a $^3n\pi^*$ doorway state, which is followed by relatively slow internal conversion to the lowest-energy and long-lived $^3\pi\pi^*$ state, possibly with simultaneous vibrational cooling in the $^3\pi\pi^*$ state. The unity triplet yield measured in this study is larger than those reported for dtThy and dtUra.[21,22] Therefore, it is demonstrate that the increased efficacy of dtPur against epidermoid carcinoma cells[23] relative to dtThy and dtUra correlates with both the longer magnitude of its triplet decay lifetime and with the larger magnitude of its triplet yield.

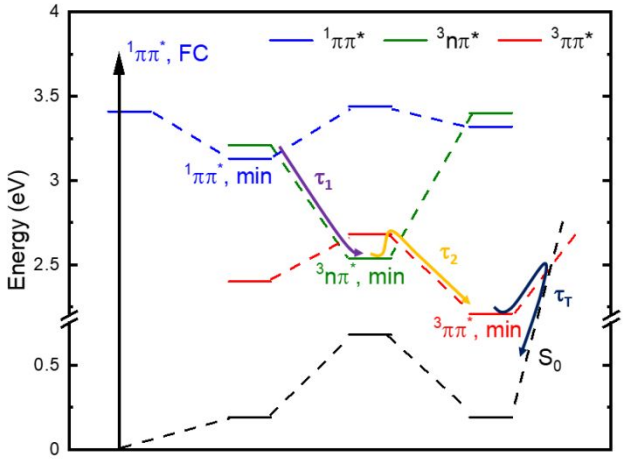

Scheme 1. Proposed deactivation mechanism of dtPur upon UVA excitation in phosphate buffer pH 7.4. Radiative deactivation pathways are omitted from the scheme due to their negligible contribution

Author Contributions

Luis A. Ortiz-Rodríguez: investigation, formal analysis, writing-original draft, writing review and editing
Sean J. Hoehn: investigation, writing review and editing
Chris Acquah: investigation, writing review and editing
Nadia Abbass: investigation, writing review and editing
Lidia Waidmann: investigation, writing review and editing
Carlos E. Crespo-Hernández: conceptualization, funding acquisition, project administration, resources, supervision, visualization, validation, writing-review and editing

Conflicts of interest

There are no conflicts to declare.

Acknowledgements

The authors acknowledge funding from the National Science Foundation (Grant No. CHE-1800052). L.A.O-.R. also acknowledge the NSF-AGEP and the NOA-AGEP programs for support. This work made use of the High-Performance Computing Resource in the Core Facility for Advanced Research Computing at Case Western Reserve University.

References

1 B. Zhao and Y.-Y. He, *Expert Rev. Anticancer Ther.*, 2010, **10**, 1797–1809.

2 G. P. Guy, S. R. Machlin, D. U. Ekwueme and K. R. Yabroff, *Am. J. Prev. Med.*, 2015, **48**, 183–187.

3 WHO, *European code against cancer*,International Agency of Research on Cancer, Lyon, 2015.

4 Global Burden of Disease Cancer Collaboration, *JAMA Oncol.*, 2019, **98121**, 1749–1768.

5 C. Morton, C.A., Szeimies, R.M., Basset-Seguin, N., Calzavara-Pinton, P., Gilaberte, Y., Haedersdal, M., Hofbauer, G.F.L., Hunger, R.E., Karrer, S., Piaserico, S. and Ulrich, *J. Eur. Acad. Dermatology Venereol.*, 2019, **33**, 2225–2238.

6 C. A. Morton, R.-M. Szeimies, N. Basset-S´eguin, P. G. Calzavara-Pinton, Y. Gilaberte, M. Haedersdal, G. F. L. Hofauer, R. E. Hunger, S. Karrer, S. Piaserico, C. Ulrich, A.-M. Wennberg and L. R. Braathen, *J. Eur. Acad. Dermatol. Venereol.*, 2020, **34**, 17–29.

7 D. E. J. G. J. Dolmans, D. Fukumura and R. K. Jain, *Nat. Rev. Cancer*, 2003, **3**, 380–387.

8 A. P. Castano, P. Mroz and M. R. Hamblin, *Nat. Rev. Cancer*, 2006, **6**, 535–545

9 M.S. Baptista, J. Cadet, A. Greer and A. H. Thomas, *Photochem. Photobiol.*, 2021, DOI:10.1111/php.13470.

10 L. A. Ortiz-Rodrguez, C.E.Crespo-Hernández, *Chem. Sci.*, 2020, **11**, 11113–11123.

11 C. Verhille, M.; Couleaud, P.; Vanderess, R.; Brault, D.; Barberi-Heyob, M.; Frochot, *Curr. Med. Chem.*, 2010, **17**, 3925–3943.

12 B. Ashwood, M. Pollum and C. E. Crespo-Hernández, *Photochem. Photobiol.*, 2019, **95**, 33–58.

13 L. A. Ortiz-Rodríguez, C. Reichardt, S. J. Hoehn, S. Jockusch and C. E. Crespo-Hernández, *Nat. Commun.*, 2020, **11**, 1-9.

14 L. Martínez-Fernández, G. Granucci, M. Pollum, C. E. Crespo-Hernández, M. Persico and I. Corral, *Chem. - A Eur. J.*, 2017, **23**, 2619–2627.

15 M. Pollum, L. Martinez-Fernandez and C. E. Crespo-Hernandez, in *Photoinduced Phenomena in Nucleic Acids I: Nucleobases in the Gas Phase and in Solvents*, eds. M. Barbatti, A. C. Borin and S. Ullrich, Springer, Cham, Switzerland, 2015, vol. 355, pp. 245–327.

16 S. Mai, M. Pollum, L. Martínez-Fernández, N. Dunn, P. Marquetand, I. Corral, C. E. Crespo-Hernández and L. González, *Nat. Commun.*, 2016, **7**, 1–8.

17 A. Massey, Y. Z. Xu and P. Karran, *Curr. Biol.*, 2001, **11**, 1142–1146.

18 E. Gemenetzidis, O. Shavorskaya, Y.-Z. Xu and G. Trigiante, *J. Dermatol. Treat.*, 2013, **24**, 209–214.

19 O. Reelfs, Y.-Z. Xu, A. Massey, P. Karran and A. Storey, *Mol. Cancer Ther.*, 2007, **6**, 2487–2495.

20 S. W. Pridgeon, R. Heer, G. A. Taylor, D. R. Newell, K. O'Toole, M. Robinson, Y. Z. Xu, P. Karran and A. V. Boddy, *Br. J. Cancer*, 2011, **104**, 1869–1876.

21 M. Pollum, S. Jockusch and C. E. Crespo-Hernández, *Phys. Chem. Chem. Phys.*, 2015, **17**, 27851–27861.

22 M. Pollum, S. Jockusch and C. E. Crespo-Hernández, *J. Am. Chem. Soc.*, 2014, **136**, 17930–17933.

23 M. Pollum, M. Lam, S. Jockusch and C. E. Crespo-Hernández, *ChemMedChem*, 2018, **13** 1044–1050.

24 C. Reichardt, R. A. Vogt and C. E. Crespo-Hernández, *J. Chem. Phys.*, 2009, **131**, 0–15.

25 J. Snellenburg, S. Laptenok, R. Seger, K. Mullen, I. Van, J. Snellenburg, S. Laptenok, R. Seger, K. Mullen, I. V. S. G. A and R. Seger, *J. Stat. Softw.*, 2012, **49**, 1–22.

26 I. . Carmichael and G. L. Hug, *J. Phys. Chem. Ref. Data*, 1986, **15**, 1–32.

27 C. Reichardt, C. Guo and C. E. Crespo-Hernández, *J. Phys. Chem. B*, 2011, **115**, 3263-3270.

28 M. J. . T. Frisch G. W.; Schlegel, H. B.; Scuseria, G. E.; Robb, M. A.; Cheeseman, J. R.; Scalmani, G.; Barone, V.; Petersson, G. A.; Nakatsuji, H.; Li, X.; Caricato, M.; Marenich, A. V.; Bloino, J.; Janesko, B. G.; Gomperts, R.; Mennucci, B.; Hratch, D. J., 2016.

29 F. Neese, *Wiley Interdiscip. Rev. Comput. Mol. Sci.*, 2018, **8**, 4–9.

30 E. Cances; B. Mennuci; J.Tomasi;, *J. Chem. Phys.*, 1997, **107**, 3032–3041.

31 M. Barone, V.; Cossi, *J. Phys. Chem. A*, 1998, **102**, 1995–2001.

32 A. D. Becke, *J. Chem. Phys.*, 1993, **98**, 5648–5652.

33 A. D. Becke, *J. Chem. Phys.*, 1993, **98**, 1372–1377.

34 C. Adamo, G. E. Scuseria and V. Barone, *J. Chem. Phys.*, 1999, **111**, 2889–2899.

35 P. Viout, A. ; Rumpf, *Bull. Soc. Chim. Fr.*, 1959, 1123.

36 B. Pullman and A. Pullman, *Biochim. Biophys. Acta*, 1962, **64**, 403–405.

37 A. Pullman, B.; Pullman, *Adv. Hetero. Chem.*, 1971, **13**, 77–159.

38 M.-T. Chenon, R. J. Pugmire, D. M. Grant, R. P. Panzica and L. B. Townsend, *J. Am. Chem. Soc.*, 1975, **97**, 4636–4642.

39 M. A. El-Sayed, *J. Chem. Phys.*, 1963, **38**, 2834–2838.

40 M. Pollum and C. E. Crespo-Hernández, *J. Chem. Phys.*, 2014, **140**, 71101.

41 D. C. Teles-Ferreira, I. Conti, A. Nenov, I. H. M. Van Stokkum, L. Ganzer, C. Manzoni, M. De Paula, G. Cerullo and M. Garavelli, *Chem. - A Eur. J.*, 2020, **26**, 336–343.